The NOAA FM-CW Snow-Level Radar

PAUL E. JOHNSTON AND JAMES R. JORDAN

*Cooperative Institute for Research in Environmental Sciences, University of Colorado Boulder, and NOAA/Earth
System Research Laboratory/Physical Sciences Division, Boulder, Colorado*

ALLEN B. WHITE

NOAA/Earth System Research Laboratory/Physical Sciences Division, Boulder, Colorado

DAVID A. CARTER AND DAVID M. COSTA

*Cooperative Institute for Research in Environmental Sciences, University of Colorado Boulder, and NOAA/Earth
System Research Laboratory/Physical Sciences Division, Boulder, Colorado*

THOMAS E. AYERS

NOAA/Earth System Research Laboratory/Physical Sciences Division, Boulder, Colorado

(Manuscript received 17 March 2016, in final form 25 August 2016)

ABSTRACT

A vertically pointing radar for monitoring radar brightband height (BBH) has been developed. This new radar utilizes frequency-modulated continuous wave (FM-CW) techniques to provide high-resolution data at a fraction of the cost of comparable pulsed radars. This S-band radar provides details of the vertical structure of precipitating clouds, with full Doppler information. Details of the radar design are presented along with observations from one storm. Results from a calibration using these storm data show the radar meets the design goals. Eleven of these radars have been deployed and provide BBH data in near–real time.

1. Introduction

NOAA ESRL scientists have a long history in studying storms on the U.S. West Coast. One result of this research is the Hydrometeorology Testbed (HMT) Legacy project between ESRL and the California Department of Water Resources (CA-DWR) (White et al. 2013). One goal of HMT Legacy was the development of a less expensive radar to provide snow-level measurements during precipitation events. This development resulted in the snow-level radar (SLR).

One parameter important in both hydrology and meteorology is the freezing level. This is especially true in complex terrain, where spatial and temporal variations of the freezing level make hydrologic forecasting difficult (Lundquist et al. 2008). Research conducted under NOAA's HMT (NOAA 2015a) shows that the brightband height (BBH), as measured by surface radars, is a good indicator of this level (White et al. 2010). Work by NOAA with the HMT showed that vertically pointing radars provide valuable information about the freezing level by measuring BBH. Existing wind profilers (Carter et al. 1995) and pulsed S-band precipitation-profiling (S-PROF) radars (White et al. 2000) are too expensive to deploy at the density required to adequately monitor the BBH. To address this problem, engineers from the CIRES and ESRL set out to construct a comparatively inexpensive vertically pointing S-band radar. The result of this development is the NOAA frequency-modulated continuous wave (FM-CW) SLR.

These FM-CW radars were designed specifically for snow-level determination, using CIRES and NOAA's expertise in developing profiling radars. Some FM-CW techniques used here were developed by the NOAA Wave Propagation Laboratory in the 1970s (Chadwick et al. 1976). Modern electronics and signal processing techniques make FM-CW technology easier to use in today's radars.

Corresponding author e-mail: Paul E. Johnston, paul.e.johnston@noaa.gov

FIG. 1. The Colfax SLR 8 Dec 2009. The TX antenna is in the shroud on the right. The radar electronics are located in the enclosure between the antennas.

A prototype SLR was installed at a site in the northern Sierra Nevada city of Colfax, California (Placer County), in December 2008. This system demonstrated the ability of a low-power (220 mW) SLR to observe the brightband and vertical structure of precipitating systems overhead. The next-generation SLR, designed with large antenna shrouds (see Fig. 1), was installed at the Colfax site in November 2009.

2. Description of the FM-CW technique

FM-CW radars have been used to study the atmosphere for many decades. Strauch (1976) demonstrated the use of FM-CW radars to obtain Doppler velocities from atmospheric targets. This work at the NOAA Wave Propagation Laboratory [predecessor of the NOAA ESRL's Physical Science Division (PSD)] is the foundation of the SLR. Transmission and reception are continuous in an FM-CW radar and thus continuous wave. Range information comes from modulating the transmitted frequency and then demodulating the received signal to get information about the range to targets observed by the radar.

Figure 2 shows a conceptual drawing of the operation of an FM-CW radar. The solid line in Fig. 2a shows the frequency of the transmitted signal as a function of time. The dashed line shows the frequency of the received signal from a target some distance from the radar. Since the radar is limited to finite frequencies, and Doppler information is desired, the frequency sweep is repeated at regular intervals, specified by the inter-sweep period T_{ISP}. During the sweep period, the transmitted radar frequency f_{TX} is specified by a simple linear relationship,:
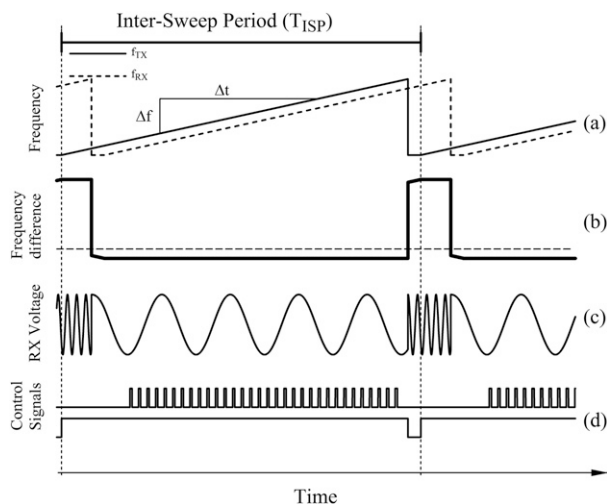

FIG. 2. Conceptual diagram showing the operation of a basic FM-CW radar. (a) The solid line is the transmitted frequency. The dashed line shows the received frequency from a fixed target. It is the same as the transmitted frequency, delayed by the propagation time to the target and back to the radar. (b) Difference between the transmitted and received frequencies for a single target. (c) Difference frequency as a voltage as it would appear at the receiver output. (d) Radar control signals that determine the ISP and the sampling times of the digitizer.

$$f_{TX}(t) = \frac{\Delta f}{\Delta t} t + f_{Start} = Mt + f_{Start}. \quad (1)$$

The received frequency f_{RX} from a target is a replica of the transmitted signal, delayed by the propagation time from the transmit antenna to the target and back to the receive antenna Δt_1, as shown in Fig. 2a,

$$f_{RX}(t) \propto f_{TX}(t - \Delta t_1) = f_{TX}(t) - M\Delta t_1. \quad (2)$$

This can be converted to range using the speed of light c. Subtracting the received frequency from the transmitted frequency gives the frequency difference Δf, which is proportional to the distance to the targets r_0,

$$\Delta f = f_{TX}(t) - f_{RX}(t) = M\Delta t_1$$
$$r_0 = \frac{c}{2}\Delta t_1 = \frac{c}{2M}\Delta f. \quad (3)$$

Since the radar repeats the sweep, it is clear in Fig. 2b that there is a period just after the sweep ends and the next sweep starts when the frequency difference is not the desired value and that the data should not be sampled. Signals that control the sweep and the data sampling are shown in Fig. 2d.

Figure 3 shows the block diagram of a basic FM-CW radar. A frequency swept signal is generated and split between transmit and receive functions. This signal is amplified and transmitted out of the radar through the
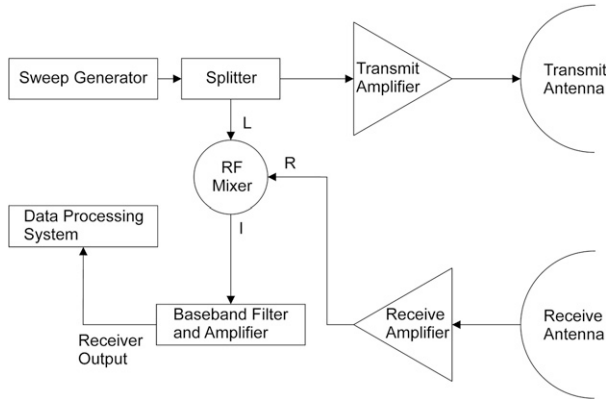
FIG. 3. Block diagram of a basic FM-CW radar.

transmit antenna. The reflected signals are received through the receive antenna and amplified. In the center of the diagram is a radio-frequency (RF) mixer that functions as an analog multiplier. By multiplying the received signal by the transmitted signal, the result is that at the output of the mixer there are two terms. The first term, the sum of the received and transmitted signal, is easily filtered out, where

$$\cos(2\pi f_{TX} t) \cos(2\pi f_{RX} t) = \frac{1}{2} \{\cos[2\pi t(f_{TX} + f_{RX})]$$
$$+ \cos[2\pi t(f_{TX} - f_{RX})]\}. \quad (4)$$

The second term is the difference of the transmitted and received signals. Equation (3) shows that this frequency difference is related to the range of the target, with larger frequencies coming from targets that are farther from the radar.

As shown in Fig. 2, a repetitive waveform is transmitted. During each sweep, the analog voltages are sampled and converted into digital values. A discrete Fourier transform (DFT) is used to transform the data into different frequencies, corresponding to different ranges. This transform takes real-valued input samples and outputs complex-valued samples that represent both the amplitude and phase of the signal. This output array of complex samples is equivalent to data array created by the analog-to-digital processing of a pulse Doppler radar from one pulse. Each complex sample represents the signal from a single range for this frequency sweep. Strauch (1976) showed that the phase at a given frequency is related to the range to the target for that sweep. The phase changes as the target slowly moves toward (or away) from the radar. This change of phase from sweep to sweep then is a measure of how far the target moves from sweep to sweep, giving the Doppler velocity of the target. Taking the data from each range over many sweeps, another DFT is done to

measure the Doppler velocity of the targets at each range, just as was done in PSD's pulsed radars. This is the double-DFT technique described by Barrick (1973).

Meteorological applications of radar involve volume scattering from aerosols, clouds, hydrometeors, or clear-air turbulence. For volume scattering, received power is proportional to the range resolution Δr of the radar. With all parameters equal (resolution, average power, antenna area, etc.), pulsed radars can be more sensitive than simple homodyne FM-CW radars (explained in appendix A). The problem is that as the range resolution gets smaller and smaller, pulse radars become very expensive, since peak powers must go up to keep average power the same. Digitization rates also increase to resolve the shorter pulses. In an FM-CW radar, the transmitted bandwidth increases to reduce range resolution, but the received bandwidth stays the same so the digitization rate can stay constant. Some FM-CW radars used for atmospheric measurements utilize resolutions as small as 0.5 m (McLaughlin 2003). The SLR normally operates with a more modest 40-m resolution, but it can operate with as small as a 12-m resolution.

3. The SLR

The SLR is a Doppler FM-CW radar with an output power of approximately 1 W. Using PSD's previous experience measuring BBH with profiling radars, the SLR design goal was to observe at least $10 \, dBZ_e$ echoes at 5 km. The SLR operates in the same frequency band as the S-PROF radars (2.8–3.0 GHz). Utilizing lower average power and smaller antennas, the SLRs are not as sensitive as S-PROF radars (see appendix A). By using S band, these radars easily observe rain and snow but do not suffer from significant attenuation during heavy rain, as do higher-frequency radars.

The SLR uses some of the same hardware and software components used in the pulsed S-PROF and wind-profiling radars. This reduced the cost and time required to develop this new radar. SLR data are recorded in the same format as our pulsed-radar data, allowing for the use of existing tools to analyze and display the data. Snow-level determination is done using the automated algorithm (White et al. 2001) developed by NOAA and CIRES (White et al. 2002).

In a traditional FM-CW radar (Fig. 3), the information at the closest ranges is at very low frequencies, requiring long observation periods to measure accurately. To make good Doppler measurements, the sweep rate needs to be fast enough to permit reasonable Doppler velocities to be measured. At S band, a Nyquist velocity of $\sim 25 \, m \, s^{-1}$ necessitates the time between Doppler samples be approximately 1 ms. To get data
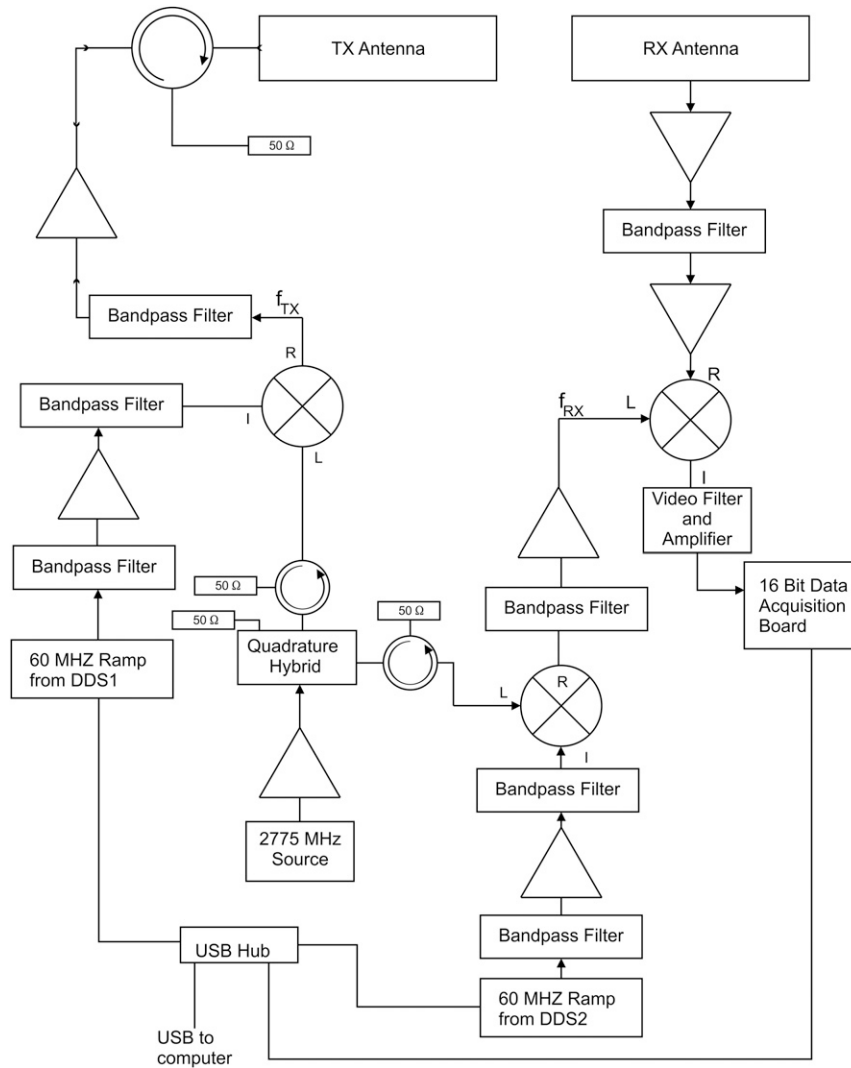
FIG. 4. Block diagram of SLR electronics.

from close to the radar, where frequencies can be less than 1 kHz, samples need to be much more than 1 ms apart. These requirements are in opposition to each other: in order to get good response from very close targets, data from small frequencies need to be measured, while to get good Doppler measurements, the length of the sweep is limited. An additional problem discovered in the SLR prototype is that the major ground clutter contributions to the signal occur at very low frequencies (close to radar). These echoes can saturate the receiver and limit the ability of the radar to make any observations. To help solve these problems, the basic FM-CW radar has been modified to utilize a frequency offset between the transmit and receive frequencies: $F_{RX} = F_{TX} + F_{OFFSET}$, as suggested by Chadwick and Strauch (1979).

By extending the analysis of Strauch (1976), it can be shown that if the offset frequency has a constant phase relationship with the transmitted signal, then full Doppler measurements can be preserved. This means that at zero range, the output of the receiver becomes

$$S_{RX}(r = 0, t) \propto F_{RX} - F_{TX} \propto A \cos(2\pi F_{OFFSET} t + \varphi_{OFFSET}).$$
(5)

Using this offset, the frequency of targets close to the radar can be set to any frequency. The SLR uses an offset of about 20 kHz, which allows for full Doppler processing for all heights and good signal at low heights.

a. Radar hardware

The SLR is constructed utilizing many commercial products. The radar is mounted on a standard 12-ft
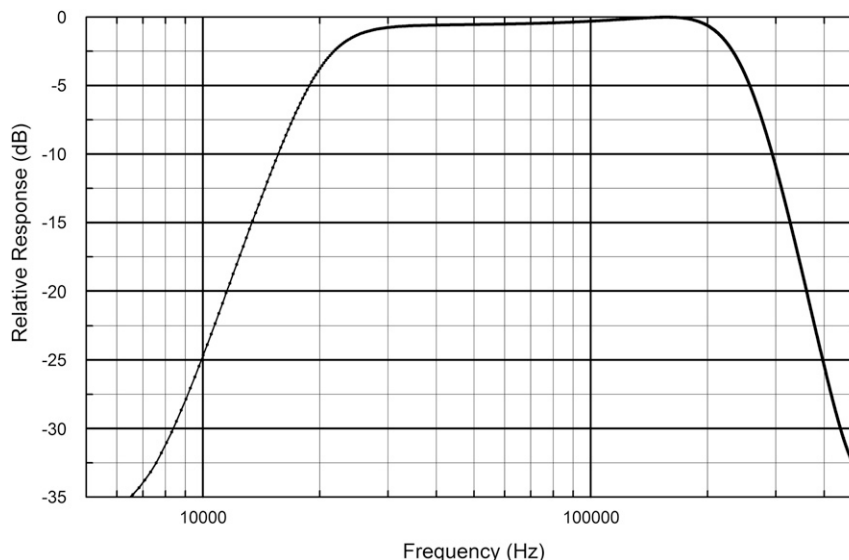
FIG. 5. Baseband filter response obtained by driving the receiver with a broadband noise source.

utility trailer, shown in Fig. 1. The antennas are located inside the two covered shrouds. Between the two antennas, a small enclosure is used to house the radar electronics. On the door of this enclosure is mounted a heating–cooling unit. The environment inside the enclosure is kept in the 18°–28°C range, comparable to temperature in an office, allowing for the use of commercial-grade electronics, reducing the cost. The SLR requires one standard 15-A, 120-V circuit for operation.

Figure 4 shows the block diagram of the SLR. Communication between the computer and the radar electronics is done using USB serial protocol. A commercial 16-bit analog-to-digital (A/D) data acquisition unit is used to acquire the data. This A/D board is located in the box with the radar electronics. Radar timing control is done using a timing board residing in the radar computer.

The receive (RX) and transmit (TX) linear sweeps are created using two direct digital synthesizers (DDSs) operating with a center frequency of 60 MHz. These signals are then mixed with a 2775-MHz stable local oscillator (STALO) to create the frequency sweeps centered at 2835 MHz. The DDSs are synchronized so there are constant frequency and phase differences between transmit and receive frequencies, maintaining Doppler capability. These are shown as two separate devices for clarity in Fig. 4, in practice the two DDSs are in one unit.

Isolation between transmit and receive signals is critical in an FM-CW radar. When there is not enough isolation, the transmit signal causes the receiver to saturate so the desired signals cannot be detected. The minimum isolation requirement for the system is 85 dB. Isolation between the transmit and receive ports of the electronics is more than 150 dB. When installed in a radar, the isolation between transmit and receive signals is more than 105 dB. These values are measured using the radar system. Using a 90-dB attenuator, the transmit signal can be put into the receiver to establish a reference level. The isolation of the electronics is then measured with the receive and transmit ports terminated with resistive loads. The transmit-to-receive isolation of the system is measured by comparing the received signal to this reference signal. Since there are contributions from ground clutter also in this received signal, we are able only to state that the isolation is more than 105 dB, the value of the measured signal including ground clutter.

One problem encountered with the S-PROF pulsed radars occurs when snow falls on the radar. When the snow on the antenna starts to melt, the antenna becomes very wet and attenuates the signals of the radar. In the SLR, the antennas are placed in shrouds with steep (45°) covered openings. This keeps the snow from accumulating on the antenna. It also helps the system achieve high isolation between transmission and reception. The antennas are 1.2-m parabolic reflectors illuminated by linear-polarized microstrip patch antennas.

Figure 5 shows the filter response for the SLR baseband filter. An advantage of using a frequency offset is that this filter can be designed with fewer compromises than in a traditional FM-CW radar. The closest ranges
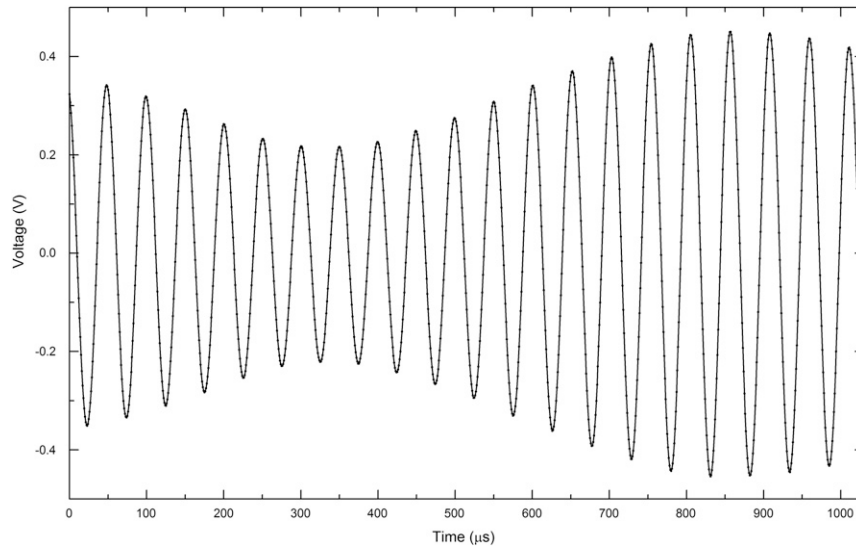
FIG. 6. Received signal from FM-CW radar. The dominant signal is from ground clutter very close to the radar.

are affected by the lowest frequency part of this response. The high-frequency response determines the maximum number of ranges and the maximum range of the system. This filter was designed so the closest ranges are in the 10–20-kHz frequency range. The high-frequency response is set so that the maximum range is about 10 km with 40-m resolution. The high-frequency

response is also set to minimize frequency aliasing when sampled at 1 MHz.

At SLR sites with large ground clutter, the offset can be used to set the first gate to a lower frequency so the clutter signal is well within the dynamic range of the system. An example is the received signal shown in Fig. 6. Here the return signal is dominated by ground
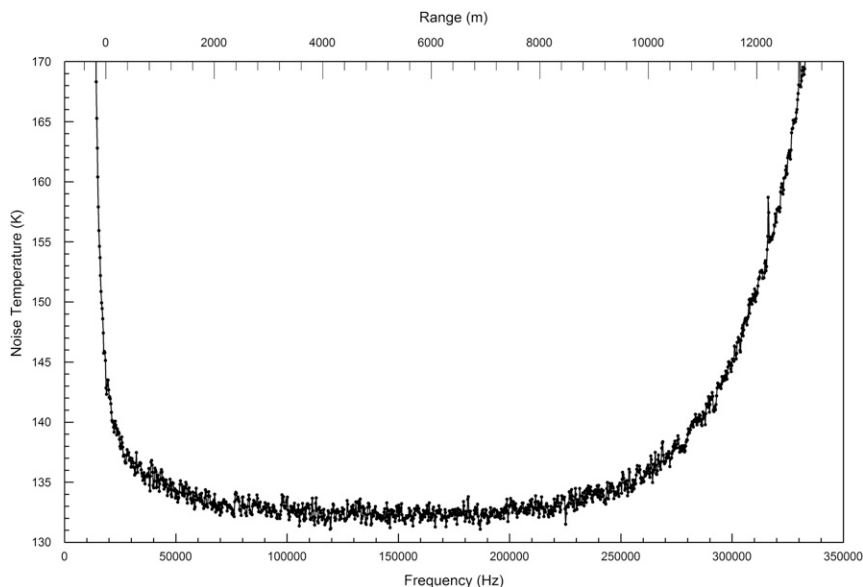

FIG. 7. Noise temperature of a typical SLR. At low frequencies, oscillator phase noise dominates. At large frequencies, there is not enough gain to maintain the noise performance. The lower x axis shows the received frequency difference and for the top one, the frequencies have been converted to range for a radar using 40-m resolution and a frequency offset of 18.5 kHz.
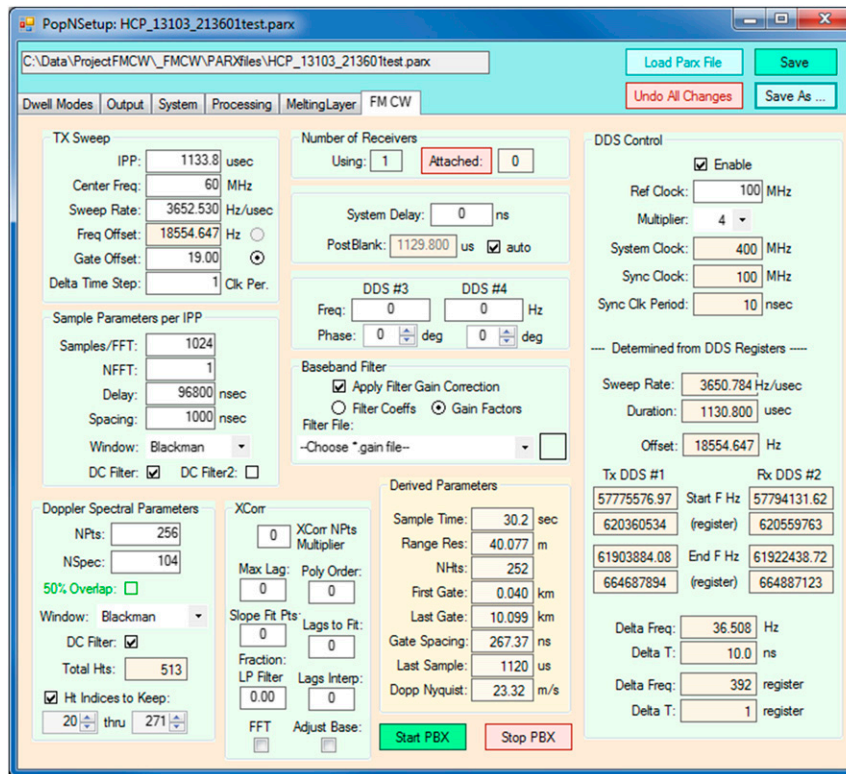
FIG. 8. Software setup screen showing typical operating parameters for the SLR.

clutter within 60 m of the radar. The SLR was operating with a range resolution of 40 m. An offset frequency of 18.55 kHz was used, reducing the TX leakage signal by 5.5 dB (a reduction by a factor of 1/3.5). The ground clutter signal shown here is at 19.7 kHz. In this example, the input signal is much smaller than the full scale ±10 V of the A/D converter. Using an offset frequency allows measurements close to the radar. In this example, data from 0 to 40 m are in the frequency range of 18.55–19.52 kHz. In conventional FM-CW radar, these data would be in the frequency region between 0 and 950 Hz, where it is very difficult to make good measurements while maintaining full Doppler capability.

Figure 7 shows the noise temperature of the receiver for a typical SLR. Near to the offset frequency (zero in this case), oscillator phase noise dominates the noise. At high frequencies, the noise performance degrades as the gain drops. A range scale corresponding to an 18.5-kHz offset frequency has been added at the top of Fig. 7. Over the 10-km range of interest normally used, the receiver noise is below 140 K. Measurements of the antenna temperature show that antenna-plus-sky noise is about 70 K. This gives a total system noise temperature less than 210 K. In the SLR, this thermal noise determines the noise level in the radar,

determining the sensitivity of the radar, as described in appendix A.

b. Software and processing of the data

The software used for the SLR has been written at PSD. After digitizing the received data, the data from each sweep are converted from frequency to range (time delay) using a DFT. The data from each sweep are then a complex array of voltages as a function of range, which is the same form as the data from one pulse of the PSD's pulsed Doppler radars. The rest of the data processing follows the same sequence of the PSD pulsed radars: take data from multiple sweeps (pulses) to create a time series; utilize DFTs to create a power spectrum at each range and then average power spectra for a dwell period; analyze the averaged power spectra to get moments representing the noise level, signal power, radial velocity, and spectral width at each range (Carter et al. 1995; Riddle et al. 2012). The moments data are then used as inputs to the snow-level algorithm (White et al. 2002, 2001).

One difference between a pulsed radar and an FM-CW radar is that gain in an FM-CW radar is not constant with range. One addition to the software is the ability to use a response curve, such as Fig. 5, to normalize the
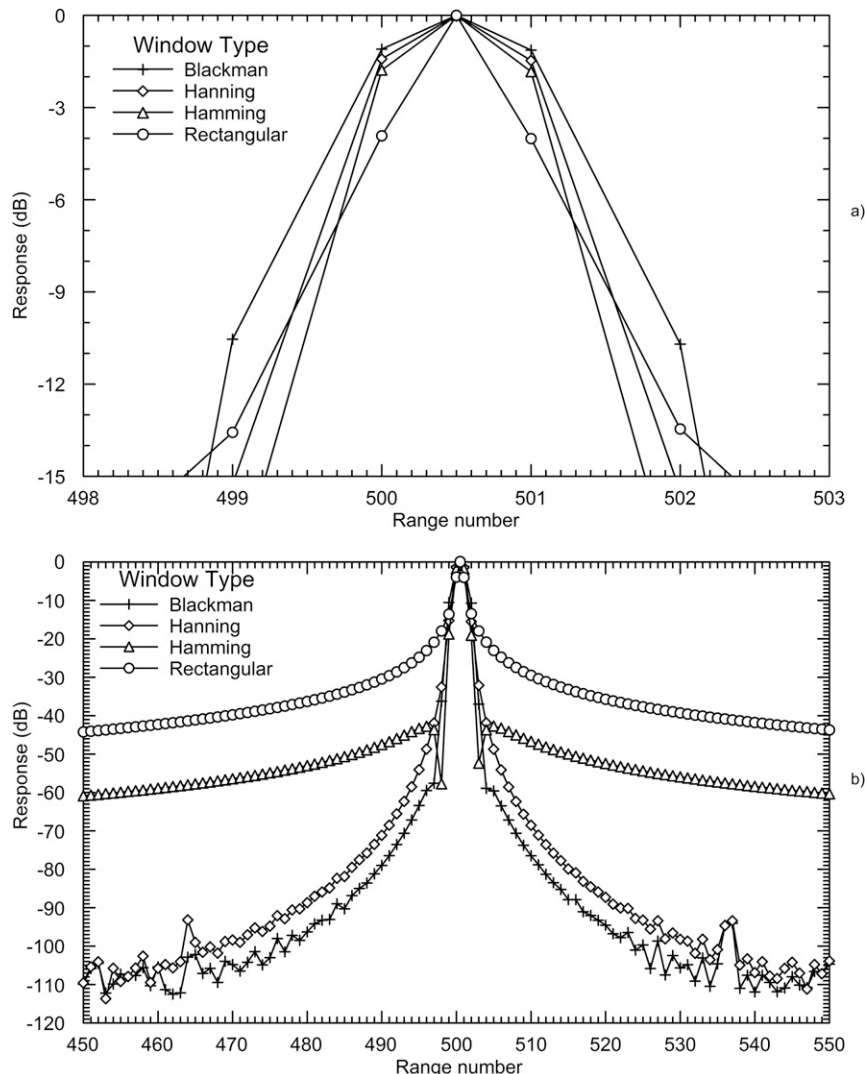
FIG. 9. Range response of SLR to different window functions in DFT. All curves are generated from the same input time series. (a) Response close to the target. (b) Response over many points of the DFT. In the SLR, each point represents a different range. The point at point 500.5 has been added based on theory to provide a reference point for the curves.

data from all ranges to the same gain value. This is done in the software as part of the normal operation.

The user interface to the software is shown in Fig. 8. Typical operating parameters are shown. White boxes show user settable parameters. Boxes with shaded backgrounds show parameters computed by the software. Other tabs in the setup screen are used to specify site location, data output locations and format, and other values required for the operation of the radar.

During testing of an SLR, the transmitter output is connected to the receiver input through an 86-dB attenuator and a short cable. This creates a large signal

that is in the linear range of the system. The normalized response from different windows applied to the same input time series is shown in Fig. 9. For this test 4096 samples were taken each sweep. The frequency offset of about 122 kHz was chosen to give equal response between 500 and 501, putting the offset frequency midway between these points. Figure 9a shows the normalized response close to the peak. The point at 500.5 has been manually inserted to show where the peak signal occurs. As expected, the rectangular window has the narrowest response and the Blackman window gives the widest response, close to the peak [for details about window functions see Harris (1978)]. In an FM-CW radar, these
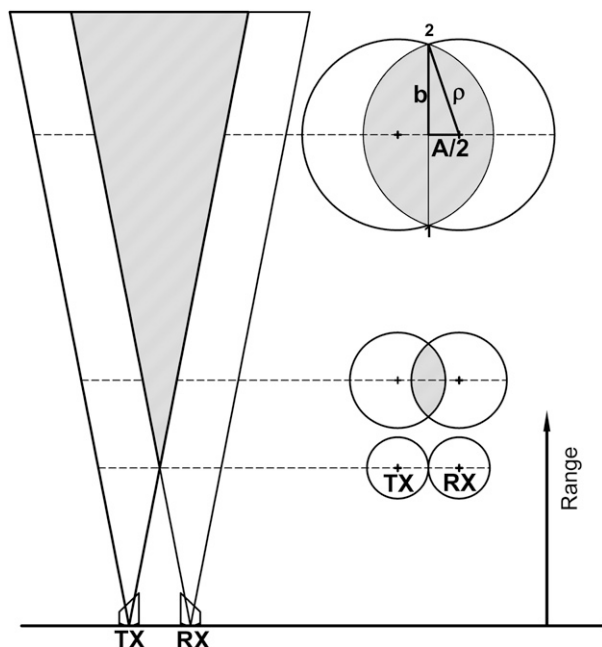
FIG. 10. Conceptual drawing of the volume reduction problem. On the left, a side view of the radar is shown. The shaded area shows the intersection of the transmit and receive antenna beams. On the right, a top view of the antenna beams at different levels are shown. Variables used in appendix B are shown in the highest range.

curves represent the range-weighting function of the radar, as well as the Doppler response weighting. Figure 9b shows the windows over the full dynamic range of the instrument. At ranges far from the peak, the situation reverses, with the rectangular window leaking into many ranges, while the Blackman window has

minimal leakage into other ranges. The other windows show different characteristics. Operationally, we use the Blackman window to minimize leakage into adjacent ranges or velocities. Figure 9b shows the SLR has more than 100 dB of dynamic range. About 36 ranges above and below the peak, a spurious signal appears as a local peak about 10 dB above the curve. This spur is instrumental and not related to the window function. At about 59 dB below the peak of the Blackman window, the response changes. This is believed to be phase noise related to the RF sources in the system. This effect is smaller than the dynamic range of our targets, so it does not affect the data.

4. Radar calibration

One way to calibrate a radar is to carefully measure all of the terms in the radar equation and use the results to get calibrated values of reflectivity. In an FM-CW radar with two antennas, this becomes difficult. Another way to calibrate a system is to use a transfer standard, using data from a different system to do the calibration. With the SLR, reflectivity is used to estimate rainfall and to compare it with an independent measurement of the rainfall as a transfer standard.

In a radar equation for volume scattering, the assumption is made that the scatters fill the volume of the radar beam. The along-beam dimension of the volume is the range resolution, Δr. The across-beam dimensions of the scattering volume are determined by the antenna characteristics. Since this is a bistatic system, the cross-range dimension of the common volume changes with range, since transmit and receive antenna beam volumes
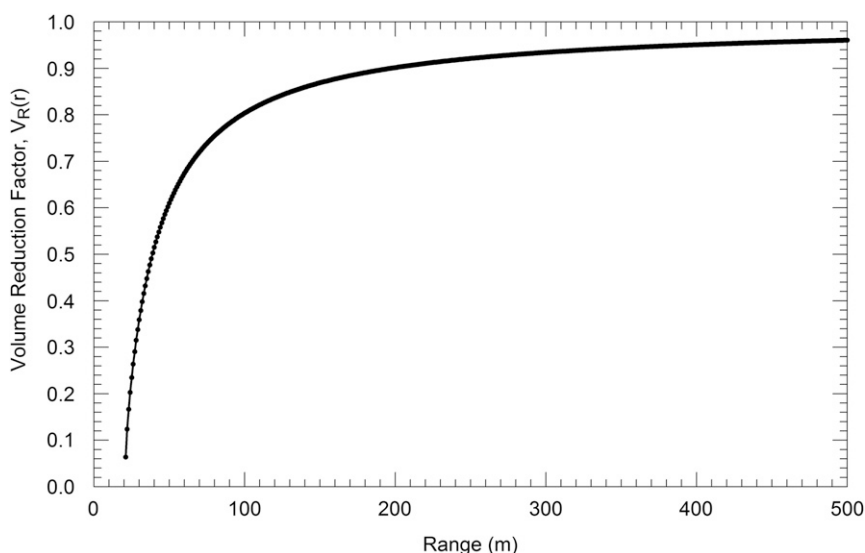

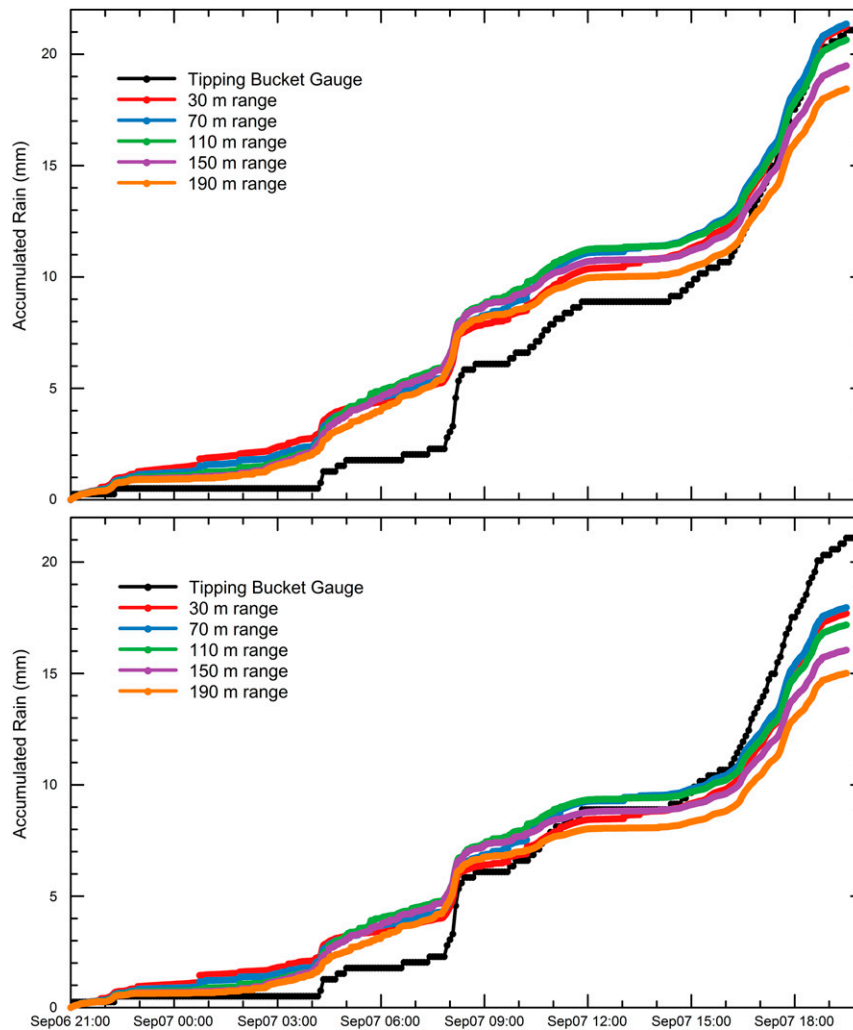FIG. 11. The term VR(r) close to the SLR.

FIG. 12. Rain accumulation for 6 and 7 Sep 2011 in Boulder. The tipping bucket gauge results are in black and the amounts at the different range gates are in color: 30 (red), 70 (blue), 110 (green), 150 (purple), and 190 (orange) m. (top) Rain accumulation using a stratiform *Z–R* relationship (bottom) the convective *Z–R* rain accumulation with the same radar constant.

do not completely overlap. Close to the radar, the transmitted energy and the received field of view have very little overlap. A full analysis of this is a difficult problem, as this is also the near-field region of the antennas. Using a $2D^2/\lambda$ criteria, the near field of the antennas extends to 27 m in this system. To simplify the problem and analysis, the antenna patterns are assumed to be cones with vertices at the center of the antennas. This is shown in the conceptual drawing in Fig. 10, which shows the common volumes as a shaded region. On the left in Fig. 10, cones representing the antenna beams are shown. On the right in Fig. 10, a top view of three ranges is shown. Using this simple geometry, a volume reduction term $V_R(r)$ can be constructed to correct for the mismatched overlap of the transmit and receive antenna

beams. Using this model with SLR values, it is found that there is no overlap until the range is 20.6 m, about the same distance of the near field of the antennas. As the range increases, transmit and receive beams have more overlap. Using the range at the center of the beam r_0, the antenna beamwidth B, and the antenna separation A, $V_R(r)$ is expressed as

$$V_R(r_0) = \frac{2}{\pi}\left\{\cos^{-1}\left(\frac{A}{2\rho}\right) - \frac{A\sin\left[\cos^{-1}\left(\frac{A}{2\rho}\right)\right]}{2r_0\tan\left(\frac{B}{2}\right)}\right\}. \quad (6)$$

Figure 11 shows how $V_R(r_0)$ varies close to the radar, using the SLR values of 6° for the beamwidth and
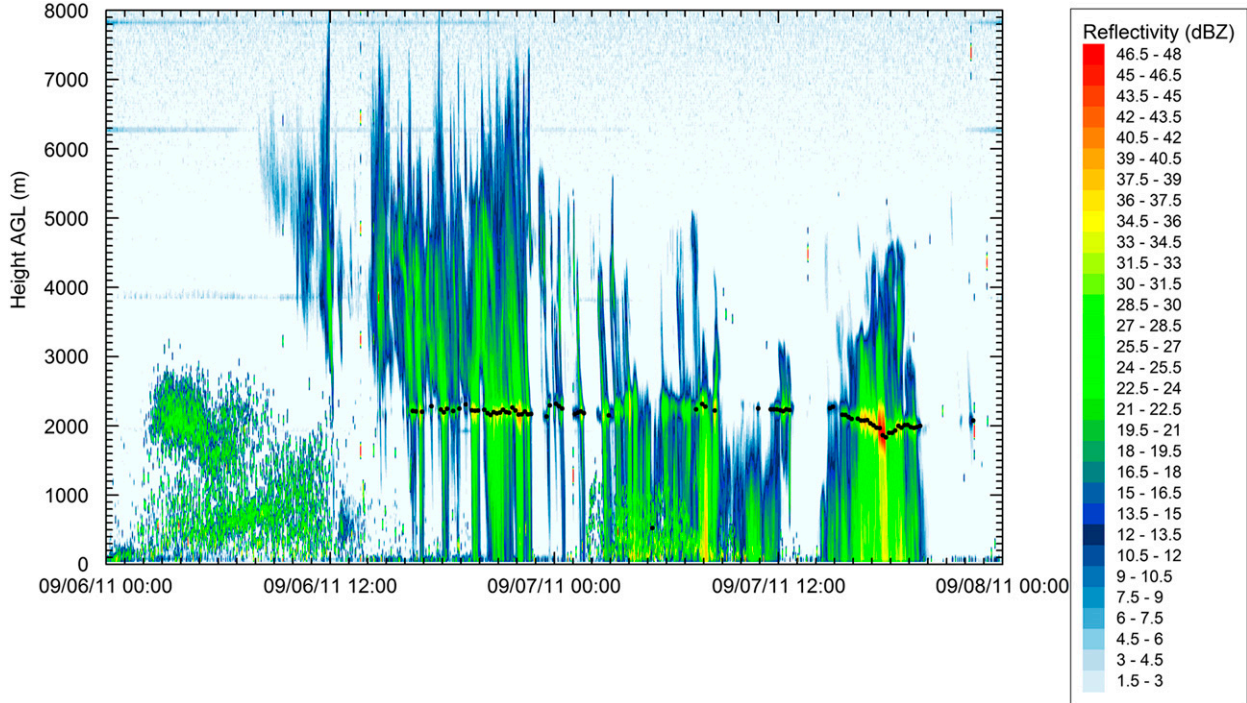
FIG. 13. Reflectivity (color legend) and melting layers (black lines) for 6 and 7 Sep 2011 in Boulder.

2.159-m separation between the antennas. The derivation of $V_R(r)$ is shown in appendix B.

Since this radar is bistatic, the transit time from the transmitter to the target and then to the receiver is not precisely the distance from the plane of the antennas to the plane of the target. For the ranges and range resolutions used in the SLR, the error is less than 0.1% when using the perpendicular distance between the antenna plane and the center of the target volume for the range.

Our experience with profiling radars shows that the noise temperature is constant, while gain varies with time and temperature. We assume noise temperature is constant and use the signal-to-noise ratio (SNR) instead of received power P_r, since it is independent of gain. At each range, the SNR is determined using only the data in that range. Since each range has the range dependent gain removed, the noise is assumed to be independent of range. To minimize variations caused by fluctuations in the noise level, the SNR at each range is recomputed using an average noise level computed from the 150 upper gates of the radar data. This reduces the variance of SNR values associated with determining the noise level independently at each range. It also removes the increases in noise at very low and high ranges associated with the increase in noise temperature observed in Fig. 8.

Calibration is done using a simple radar equation (a detailed radar equation is shown in appendix A), with most of the terms combined into one constant, D,

$$Z_e(r_0) = \frac{\text{SNR}(r_0)r_0^2}{DV_R(r_0)}. \tag{7}$$

An independent measurement of the rainfall near the SLR is used as a calibration transfer standard. From the reflectivity Z_e, there are relations that give the rain rate R (mm h^{-1}),

$$Z_e = AR^b. \tag{8}$$

Equation (8) is used to convert the reflectivity to rain rate. Parameters A and b depend on the precipitation type. This equation applies at sea level, so it needs to be modified for the density difference at heights (Ulbrich and Atlas 1998),

$$Z_1 = A_1 R_1^b = A\left(\frac{\rho}{\rho_0}\right)^{0.4b} R^b. \tag{9}$$

Density ρ is assumed to vary exponentially with a scale height of 8.55 km (Stull 2000). Solving Eq. (9) for R and inserting Eq. (7) for reflectivity gives the result used for calibration (h is range gate height above sea level),
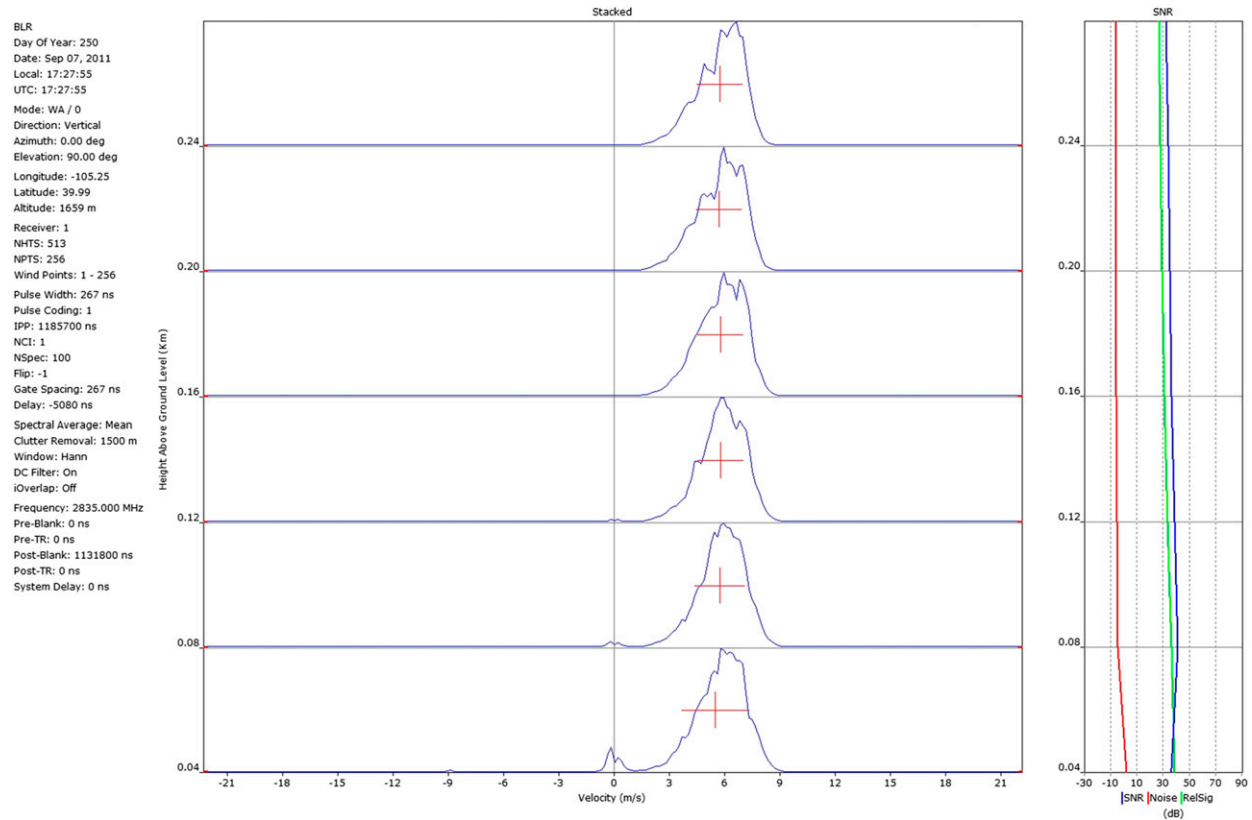
FIG. 14. Data from dwell 1727:55 UTC 7 Sep 2011: (left) velocity vs height and (right) SNR vs height. The average power spectra from the lowest six heights are shown. At each range, the spectrum was normalized, so the peak power is at the top of the plot for that range. The vertical line of the cross (+) shows the mean velocity moment, the horizontal bar shows the second moment, or the spectral width.

$$R(r_0) = \left[\frac{\text{SNR}(r_0) \times r_0^2}{D \times A \times V_R(r_0)} \right]^{1/b} e^{0.4h/8550\text{m}}. \quad (10)$$

The calibration software uses four different sets of A and b as described by Zhang et al. (2011) and is used in the national Quantitative Precipitation Estimation system. The choice of model is then determined by the storm type: either stratiform, convective, warm rain, or snow.

To establish the sensitivity of the SLR, data from an SLR located near the David Skaggs Research Center in Boulder, Colorado, is used for calibration. On 6 and 7 September 2011, 21.082 mm of rain were measured by the tipping-bucket rain gauge about 210 m from the SLR. The SLR operated using a resolution of 40 m and a time resolution of 36 s. The first gate is centered at 28.5 m above the radar. After SNR adjustments for noise level changes, Eq. (10) was used to determine D. Using an iterative procedure, D was determined such that the average accumulation of the lowest three ranges matched the rain gauge accumulation. During the rainy period of

the storm (from 2100 UTC 6 September 2011 to 1930 UTC 7 September 2011, when the rain gauge showed data), there were 2246 dwells of the radar.

The results of this calibration and the rain accumulation for these gates are shown in Fig. 12. Figure 12a shows results using the stratiform Z–R relationship (Marshall–Palmer), $Z = 200R^{1.6}$. Figure 12b shows that the rain accumulation obtained using the convective Z–R relation, with the same calibration constant, is 19.38 mm. To get the correct accumulation value using the convective Z–R relation requires an increase of the calibration value by 1.1 dB.

Radar data can vary over orders of magnitude. To accommodate this the decibel scale is used, which treats the data logarithmically. This allows Eq. (7) to be written in the form

$$\text{dB}Z_e = \text{SNR}(\text{dB}) + 20\log(r_0) \\ - 10\log[V_R(r_0)] + F. \quad (11)$$

Term F has a value of -53.81 dB for the stratiform calibration, or -52.83 dB for the convective calibration.
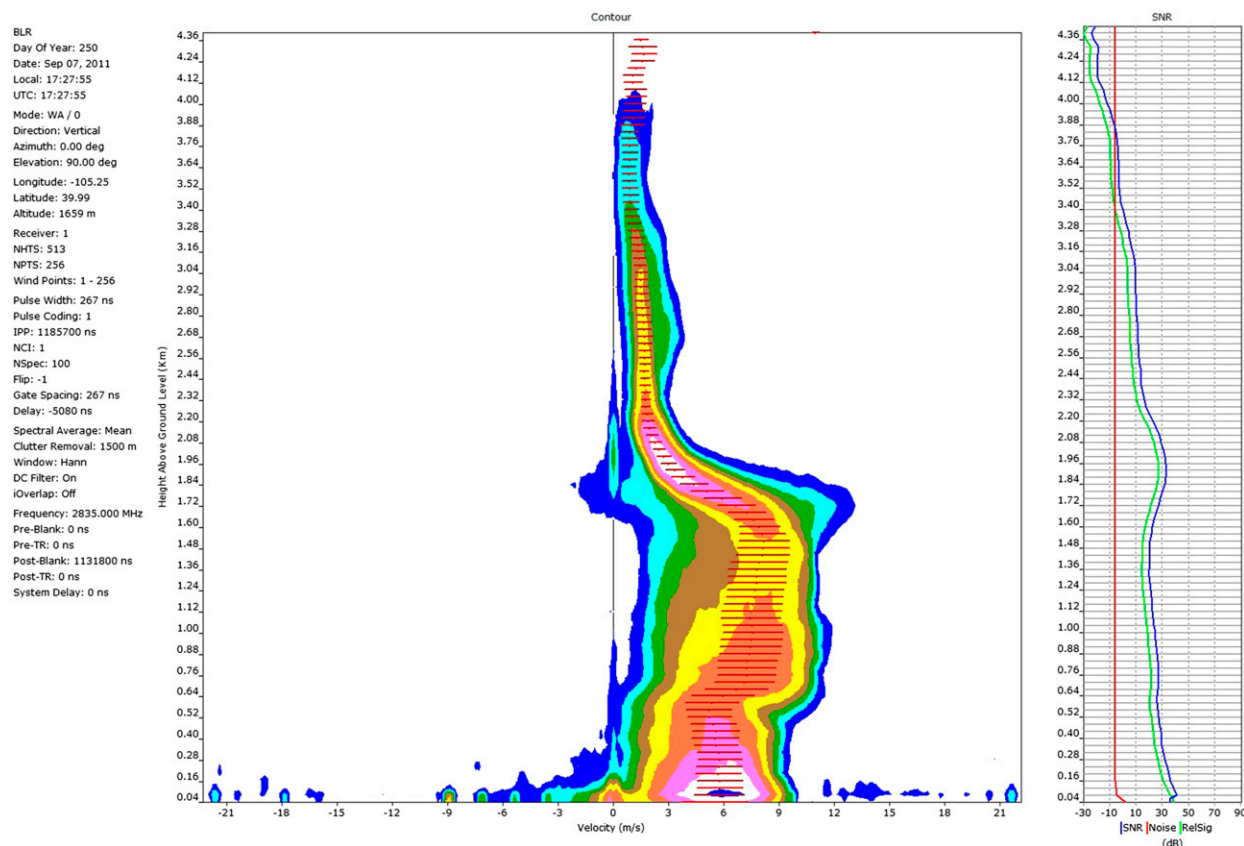
FIG. 15. Data from dwell 1727:55 UTC 7 Sep 2011: (left) velocity vs height and (right) SNR vs height. The bottom contour is 3 dB above the local noise floor. Contour interval is 6 dB.

A better calibration might be achieved by using the convective data for the first part of the storm and stratiform for the second part, or by using different Z–R relationships. This calibration is done to get an estimate of the radar sensitivity and not a definitive calibration.

Reflectivity data (using a stratiform calibration constant) for 7 and 8 September are shown in Fig. 13. The storm appears overhead several hours before the rain starts at the surface. Prior to the storm, the radar observes bioscatter from birds, bats, or insects in the radar field of view. The time scale is in UTC: local sunset occurs at about 0224 UTC and local sunrise is at about 1333 UTC, so these targets are night fliers. The faint stripes at about 3900, 6300, and 7800 m are artifacts generated by the radar electronics. Also shown in Fig. 13 are the 10-min average snow levels computed by the radar. There are three main reasons the bioscatter does not affect the snow-level determination: First, the migrating species appear to stop flying during precipitation; second, the snow-level algorithm uses profile information that discriminates against point targets; and third, the snow-level algorithm uses a consensus-average technique to produce 10-min averages.

Figure 14 shows data from the lowest six ranges during one dwell. This display was generated by the Lap-XM Console program, usually associated with pulsed radars. The pulse width was reported as 267 ns, corresponding to the 40-m range resolution of the SLR. The interpulse period (IPP) of 1185.7 μs is the sweep period of the SLR, and it determines the Nyquist velocity of the Doppler data. In this example, a noise enhancement of 8 dB is shown in the bottom gate, caused by noise internal to the radar. The bottom gate is at 28.5 m, not the 40 m reported in this image. This discrepancy is due to not having the range calibration value in the software when the data were obtained. This image also reports that a Hann window was used on the Doppler spectra. This is a minor error, since a Blackman window was actually used. The rain spectra are very clean. The 28.5-m gate shows some evidence of ground clutter at zero velocity, but it is still a very useable power spectrum. To see the data from many heights, a contour display of the spectral data (dB) is
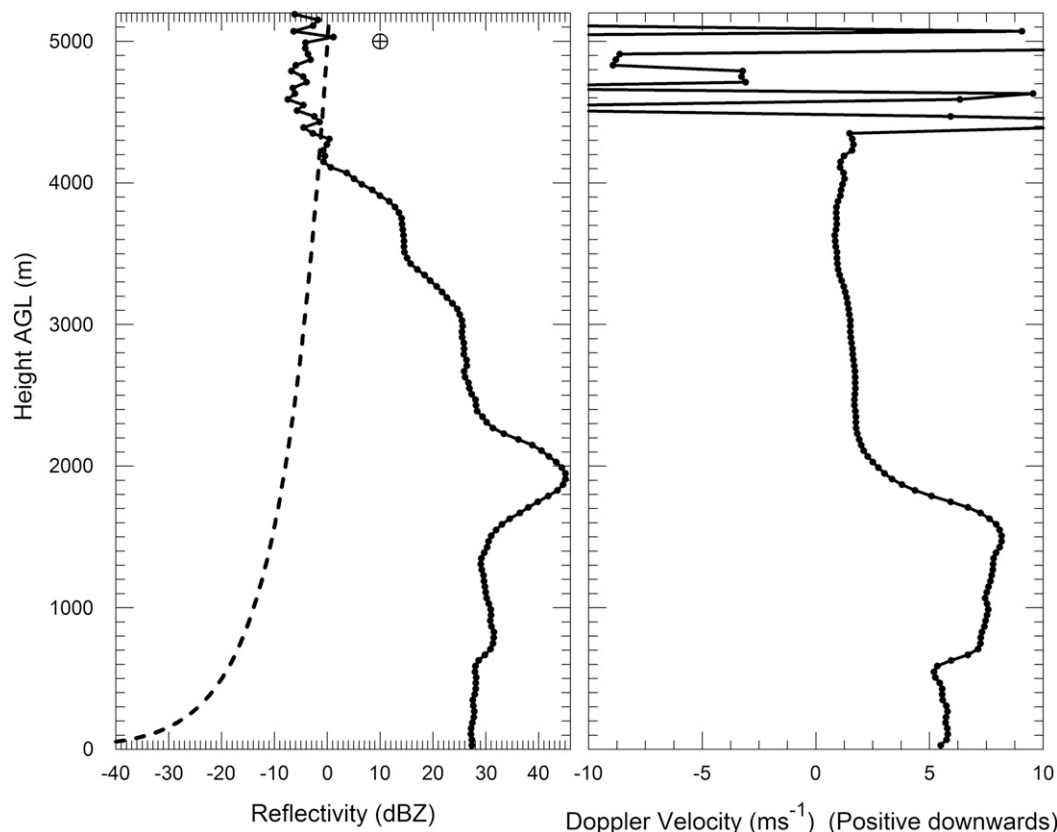
FIG. 16. Reflectivity and velocity profile from the dwell 1727:55. The dashed line shows the minimum detectable signal for this dwell. The sensitivity design goal is shown as the crossed circle ⊕ at 5000 m, 10 dBZ.

used, as shown in Fig. 15, where 110 heights are shown. The bright band is evident near 1.96 km above the radar. In this logarithmic plot, the ground clutter echo is easily observed at zero velocity in several ranges.

Figure 16 shows the reflectivity and velocity profiles from this dwell. The reflectivity values have been corrected for enhanced noise in the lower gates, the volume reduction term, and the density correction term. The 28.5-m gate is 1.5 dB smaller than the 80-m gate, suggesting that the correction terms are not fully correcting the reflectivity, or that the reflectivity is not constant over the bottom few gates. The minimum detectable signal is also shown in Fig. 16. This curve is 3 dB above the Riddle threshold (Riddle et al. 2012) for these data. Above 4300 m, the velocities become random, since the signal is not strong enough to detect. Figure 16 shows

TABLE 1. SLR locations and installation dates.

Site name	ID	Lat (°)	Lon (°)	Installation date	GPS water vapor
Colfax, CA	cff	39.08	−120.94	10 Dec 2008	Yes
Shasta Dam, CA	std	40.72	−122.43	9 Dec 2009	Yes
New Exchequer Dam, CA	ner	37.60	−120.28	3 Dec 2010	No
Pine Flat Dam, CA	pfd	36.83	−119.33	6 Dec 2010	Yes
Oroville Dam, CA	ovl	39.53	−121.49	8 Dec 2011	Yes
Happy Camp, CA	hcp	41.79	−123.39	2 Feb 2012	No
Kernville, CA	knv	35.75	−118.42	2 Jan 2012	Yes
San Bernardino, CA	sbo	34.20	−117.33	12 Mar 2013	No
San Luis Reservoir, CA	slr	37.06	−121.07	2 Apr 2013	No
Saint Helena, CA	sth	38.55	−122.49	9 Jul 2014	No
Plymouth, NH (12.7 W)	pmh	43.76	−71.69	18 Nov 2014	Yes

that the design goal of 10-dBZ sensitivity at 5-km range has been achieved.

5. Discussion and conclusions

A new snow-level radar has been developed by the Physical Science Division (PSD) of NOAA's ESRL. This inexpensive instrument uses modern electronics and signal processing in an FM-CW Doppler radar to make vertical observations of precipitating clouds. This makes it feasible to dedicate an SLR to long-term observations at a single site.

The SLR was designed to observe brightband height (BBH). The design goal has been met, with the radars easily observing 10 dBZ_e at 5 km above the radar. The hardware cost for the SLR, as shown in Fig. 1, is approximately $35K. As shown in appendix A, the SLR has comparable sensitivity to the S-PROF pulsed radar. The S-PROF hardware cost is more than 5 times that of the SLR.

Ten SLR units have been deployed in California as part of a larger observing network (White et al. 2013). The SLRs used in the California network utilize 40-m gate spacing, observing to 10 km above the radar. An eleventh SLR is deployed in New Hampshire at Plymouth State University. This SLR (11) has been modified to have 13-W output power and operates with 30-m resolution. A surface meteorological instrument system is deployed with each SLR. Some sites also have GPS water vapor measurement systems. Table 1 shows the locations of these radars.

All 11 radars communicate data in near–real time to PSD. The relative reflectivity, Doppler velocity, and BBH are available in graphical form on the PSD website (NOAA 2015b). Data in machine-readable form are also available from this website.

These units have proven to be very reliable. The most common causes of loss of data are loss of communication with the SLR, or a loss of power to the SLR. The SLR has proven ability to measure BBH levels with 10-min periods. Examination of the real-time data from the Colafax, Shasta Dam, and New Exchequer Dam profilers from installation date until the end of 2015 shows data from the radar are available for more than 92% of the time the instrument was operational.

APPENDIX A

Detectability

This appendix details the derivation of the SNR of FM-CW and pulsed radars, using the same formulation of the radar equation. Using SNR, the derivation of the detectability of the signal D_{Signal} is then shown. This allows the relative sensitivity of the two radar types to be established. Care is taken to include all factors so valid comparisons of the two radar types can be accomplished.

The textbook by Doviak and Zrnić (1993, hereafter DZ) contains a detailed derivation of the radar equation for volume scattering. Modifications were made to Eq. (4.16) in DZ to get the radar equation, Eq. (A1), used for this discussion. The four modifications involved assuming negligible path attenuation, identical transmit and receive antennas, circular symmetry of the antenna beam, and expressing Δr in terms of the pulse duration, $\Delta r = c\tau/2$. Equations (2.49) and (2.26) in Balanis (1997) were used to simplify the antenna terms, resulting in

$$\overline{P_r(r_0)} = \overbrace{\frac{P_t V_R(r_0) G_s \varepsilon^2 A_e \Delta r}{32 \ln(2) l_r}}^{\text{Radar parameters}} \times \overbrace{\frac{\eta}{r_0^2}}^{\text{Target parameters}} . \quad \text{(A1)}$$

In the pulsed radar case, $\overline{P_r(r_0)}$ is the average power received from one pulse, from a target at range r_0 with volume reflectivity η illuminated with peak transmitted power P_t. The effective antenna area is A_e, and the receiver-matched filter-loss term is l_r. The gain of the system is G_s, and the antenna efficiency is ε.

For an FM-CW radar, $\overline{P_r(r_0)}$ is the average power received from one frequency sweep, after the sweep has been transformed from frequency to range, from a target at r_0 with η illuminated with average transmitted power $\overline{P_t}$. Term $V_R(r_0)$ accounts for the bistatic geometry of the FM-CW radar, as described in the calibration section of the main text. For the FM-CW, l_r is unity. For the pulse system $V_R(r_0)$ is unity.

For both types of radars, the SNR is the ratio of the signal power to the noise power in the averaged spectrum at the end of the processing,

$$\text{SNR} = \frac{\overline{P_r(r_0)}}{P_{\text{Noise}}} = \frac{\overline{P_r(r_0)}}{G_S k T_{\text{Sys}} B_N}. \quad \text{(A2)}$$

The received power is the integrated signal value and can extend over several spectral bins. The noise is

characterized as white thermal noise, so the noise power at the output of the receiver can be expressed as a simple function of the system gain G_S, the noise bandwidth B_N, and the system noise temperature T_{Sys}. At S-band frequencies, the cosmic noise is a small fraction of the total noise, so it is included as part of the system noise.

In a pulse radar, B_N is inversely related to the pulse duration τ. The receiver output is sampled once every interpulse period T_{IPP}. The noise bandwidth is much larger than the Nyquist frequency of this sample rate, so noise is aliased into the samples. From Eq. (3.38) in DZ, the noise bandwidth of a square pulse matched to a Gaussian filter is given by Eq. (A3). SNR is maximized when $B_6 = 1.04/\tau$, as shown:

$$B_{NPulse} = \frac{1.06B_6}{\sqrt{2}} = \frac{1.06 \times 1.04}{\sqrt{2}\tau} = \frac{0.7354}{\tau}. \quad (A3)$$

For the FM-CW case, the receiver output bandwidth is determined by the baseband filter, which has a fixed bandwidth. This bandwidth is smaller than the Nyquist frequency of the sampling rate, so the noise power is not aliased. Since the SLR uses a simple homodyne receiver, there is a factor of 2 in the noise bandwidth to account for the contributions from the upper and lower side bands. A DFT converts the samples from each sweep from frequency to range. The noise bandwidth of the DFT bin determines the noise in each range gate. It is a function of the number of range samples N_{range}, the sample spacing t_{sample}, and the noise bandwidth of the window function F_3 used in the frequency-to-range transformation (see Table I in Harris 1978). Equation (A4) shows that the FM-CW noise bandwidth is independent of the range resolution of the radar,

$$B_{NFM-CW} = \frac{2F_3}{t_{Sample}N_{Range}}. \quad (A4)$$

For comparison purposes, the range resolution needs to be expressed more explicitly. To accomplish this, the range resolution r_6 will be expressed as the distance between the -6-dB points of the range weighting function. In the pulsed radar case, with a rectangular pulse matched to a Gaussian response, with $B_6\tau = 1.04$, Eq. (4.30) in DZ gives this range resolution:

$$r_{6Pulse} = \frac{1.23c\tau}{2} = 1.23\Delta r. \quad (A5)$$

For FM-CW radar, the slope of the frequency ramp M controls the range resolution. The -6-dB width, F_4, of

the window chosen for the frequency-to-range DFT affects the range resolution,

$$r_{6FM-CW} = \frac{F_4 c}{2 \times 10^6 M t_{Sample} N_{Range}} = F_4 \Delta r. \quad (A6)$$

Inserting Eqs. (A1), (A3), and (A5) into Eq. (A2) gives the SNR for the pulse radar system,

$$SNR_{Pulse} = \frac{\overline{P_r(r_0)_{Pulse}}}{P_{NoisePulse}} = \frac{P_t\varepsilon^2 A_e \Delta r}{32 \times l_r \times \ln(2) \times k T_{Sys} B_{NPulse}} \frac{\eta}{r_0^2}$$

$$= \frac{P_t\varepsilon^2 A_e r_6 \tau}{22.181 \times l_r k T_{Sys}} \frac{\eta}{r_0^2}. \quad (A7)$$

One problem remains before these equations can be used to compare the two radar types. In the pulse radar, the power is the peak value, while in the FM-CW it is the average power. Using the duty cycle of the radar (τ/T_{IPP}), peak power is converted to average power. For a matched filter in the pulse radar, l_r is 1.698 (the linear value of 2.3 dB), as discussed in DZ (p. 80). These two changes modify Eq. (A7), where

$$SNR_{Pulse} = \frac{P_t\varepsilon^2 A_e r_6 \tau}{22.181 \times l_r k T_{sys}} \frac{\eta}{r_0^2}$$

$$= \frac{P_t(\tau/T_{IPP})(T_{IPP}/\tau)\varepsilon^2 A_e r_6 \tau}{37.668 \times k T_{sys}} \frac{\eta}{r_0^2}$$

$$= \frac{\overline{P_t}\varepsilon^2 A_e r_6 T_{IPP}}{37.668 \times k T_{sys}} \frac{\eta}{r_0^2}. \quad (A8)$$

Inserting Eqs. (A1), (A4), and (A6) into Eq. (A2) gives the SNR for the FM-CW radar. The term F_5 is defined as the ratio of the sampling time to the intersweep period (ISP), $F_5 = t_{sample}N_{range}/T_{ISP}$. This is done so the FM-CW SNR equation is in terms of the sweep period, so that the Doppler resolution and Nyquist velocity can be specified when comparing with the pulse radar,

$$SNR_{FM-CW} = \frac{\dfrac{\overline{P_t}V_R(r_0)G_s\varepsilon^2 A_e \Delta r}{32 \times l_r \ln(2)} \dfrac{\eta}{r_0^2}}{G_s k T_{sys} B_{NFM-CW}}$$

$$= \frac{\overline{P_t}V_R(r_0)\varepsilon^2 A_e r_6 F_5 T_{ISP}}{44.361 \times k T_{sys} F_3 F_4} \frac{\eta}{r_0^2}. \quad (A9)$$

A way to compare radars is to solve for the D_{Signal} of the radar. This is defined (see Gage and Balsley 1978) as the ratio of the peak spectral density value S_{peak} to the average noise density fluctuation ΔS_{noise} in the averaged

power spectrum. This includes the effects of all the signal processing. In Eq. (A10), the constant A is the ratio between the peak and the signal power. There are different estimates of this value, depending on the signal model, but for this application, letting it be a constant is adequate.

The average noise fluctuation is equal to the mean noise density level $\langle S_{\mathrm{noise}} \rangle$ divided by the square root of the number of spectra averaged together, N_{Spectra} [Eq. (10) of Petitdidier et al. 1997]. The mean noise level is the total noise power divided by the number of voltage samples N_{Coherent} used to get an individual spectrum. In the FM-CW case, $N_{\mathrm{CoherentFM\text{-}CW}}$ is the number of points in the spectrum, N_{DFT}. In the pulse radar case, time-domain averaging of the samples may be done prior to the DFT processing. It is assumed here that the signals of interest are less than one-half of the Nyquist velocity, so the time-domain averaging has less

than 1-dB effect on the signal power. The means that $N_{\mathrm{CoherentPulse}}$ is the product of the number of time-domain averages N_{TDA} and the number of points in the spectrum, $N_{\mathrm{CoherentPulse}} = N_{\mathrm{TDA}} N_{\mathrm{DFT}}$,

$$
\begin{aligned}
D_{\mathrm{Signal}} = \frac{S_{\mathrm{Peak}}}{\Delta S_{\mathrm{noise}}} &= \frac{\overline{P(r_0)}A}{\left(\dfrac{P_{\mathrm{Noise}}}{N_{\mathrm{Coherent}}\sqrt{N_{\mathrm{Spectra}}}} \right)} \\
&= \frac{\overline{P(r_0)}}{P_{\mathrm{Noise}}} A N_{\mathrm{Coherent}}\sqrt{N_{\mathrm{Spectra}}} \\
&= \mathrm{SNR} \times A N_{\mathrm{Coherent}}\sqrt{N_{\mathrm{Spectra}}}.
\end{aligned}
\tag{A10}
$$

Equation (A11) shows the relative sensitivity of the two types of radar. This is the general case, with no assumptions about the radars,

$$
\frac{D_{\mathrm{SignalPulse}}}{D_{\mathrm{SignalFM\text{-}CW}}} = \frac{(\mathrm{SNR} \times A N_{\mathrm{Coherent}}\sqrt{N_{Spectra}})_{\mathrm{Pulse}}}{(\mathrm{SNR} \times A N_{\mathrm{Coherent}}\sqrt{N_{Spectra}})_{\mathrm{FM\text{-}CW}}} = \frac{\left(\dfrac{\overline{P_t}\varepsilon^2 A_e r_6 T_{\mathrm{IPP}}}{37.668 \times k T_{\mathrm{sys}}} \dfrac{\eta}{r_0^2} N_{\mathrm{Coherent}}\sqrt{N_{\mathrm{Spectra}}} \right)_{\mathrm{Pulse}}}{\left[\dfrac{\overline{P_t} V_R(r_0)\varepsilon^2 A_e r_6 F_5 T_{\mathrm{ISP}}}{44.361 \times k T_{\mathrm{sys}} F_3 F_4} \dfrac{\eta}{r_0^2} N_{\mathrm{Coherent}}\sqrt{N_{\mathrm{Spectra}}} \right]_{\mathrm{FM\text{-}CW}}}.
\tag{A11}
$$

To compare two radars, one of each type, Eq. (A11) can be simplified by making some assumptions. In an average spectrum, the velocity bin spacing Δv is a function of the radar wavelength λ, the number of samples, and the sample timing,

$$
\Delta v_{\mathrm{Pulse}} = \frac{\lambda}{2 N_{\mathrm{Coherent}} T_{\mathrm{IPP}}}
$$

$$
\Delta v_{\mathrm{FM\text{-}CW}} = \frac{\lambda}{2 N_{\mathrm{Coherent}} T_{\mathrm{ISP}}}.
$$

By assuming the two radars being compared have the same wavelength, spectral velocity spacing, average power, antenna area and losses, spatial resolution, system noise temperature, and number of spectra on average, and observe the same target, most terms in Eq. (A11) cancel, resulting in

$$
\frac{D_{\mathrm{SignalPulse}}}{D_{\mathrm{SignalFM\text{-}CW}}} = \frac{44.361 \times F_3 F_4}{37.668 \times V_R(r_0) F_5}.
\tag{A12}
$$

Putting in typical SLR values for $F_3 = 1.73$, $F_4 = 2.35$, and $F_5 = 0.93$ changes the constant from 44.361 to 193.9. Equation (A12) shows that the pulse system is more sensitive than the FM-CW system, in this comparison. At far ranges, where $V_R = 1$, a pulse system with these

assumptions would be 7.1 dB more sensitive than the equivalent FM-CW system.

In practice, radar systems are rarely identical. As an example, two radars—the Santa Rosa, California, S-PROF (STR) and the St. Helena SLR (STH)—are compared. These radars are situated about 17 mi apart in Sonoma and Napa Counties, northeast of San Francisco, California. The S-PROF radar operates in two modes, for this comparison the low-sensitivity mode parameters are shown. Table A1 shows the operating parameters. Comparing the two different radars using Eq. (A11) shows that the FM-CW radar is 0.5 dB more sensitive than the low mode of the S-PROF radar. This is a small difference, showing that these two radar systems are nearly equal in sensitivity, in these modes. Of course, the high-sensitivity mode of the S-PROF is 8.5 dB more sensitive, since it has higher average power.

APPENDIX B

Volume Reduction Term

This appendix details the derivation of VR(r), shown as Eq. (6). The term VR(r) accounts for the reduced scattering volume observed by the receiver. For our

TABLE A1. Typical operating parameters for S-PROF and SLR radars. The high-resolution mode of the S-PROF is shown.

Variable	Description	Units	STR S-PROF value (low mode)	STH SLR value
P_t	Peak transmitted power	W	300	—
$\overline{P_t}$	Average transmitted power	W	2.98	1.01
V_r	Geometry correction factor for bistatic operation		1	1
λ	Wavelength of radar	m	0.104	0.106
τ	Pulse duration	ns	417	—
l_r	Matched filter loss factor		1.698	1
ε	Antenna efficiency		0.794	0.891
A_e	Effective antenna area	m^2	2.33	0.58
T_{sys}	Noise temperature	K	300	200
t_{sample}	Sample spacing for FM-CW	μs	—	1.0
N_{range}	Number of range samples, FM-CW		—	1024
F_3	Noise bandwidth of spectral window	bins	1	1.73
Δr	Range resolution, $\Delta r = c\tau/2$	m	62.5	40
r_6	Distance between the -6-dB points in range	m	76.9	94.0
F_4	-6-dB width of range window	bins	1	2.35
Δv	Spacing of spectral points	m s^{-1}	0.12	0.18
T_{IPP}	Interpulse period	μs	42.0	—
T_{ISP}	Intersweep period	μs	—	1173.7
F_5	Ratio of FM-CW sampling time to T_{ISP}		—	0.87
$N_{Spectra}$	Number of spectra averaged		79	104
N_{DFT}	Number of points in DFT		256	256
N_{TDA}	Number of time-domain averages		42	1

analysis we model the antenna responses as vertical cones with vertices at the focal points of the TX and RX antennas. The term VR(r) is the ratio of the volume common to both beams to the volumes of the antenna response when completely overlapped. The radial dimensions of the volumes are completely matched, so VR(r) becomes the ratio of the overlapping areas at the center of the range volumes,

$$\text{VR}(r) = \frac{\text{Area of overlap}}{\text{Area of maximum overlap}}.$$

The top-right part of Fig. 10 shows the pertinent details required for the derivation of VR(r). The area of overlap is twice the area that is to one side of the chord from 1 to 2. The angle $s = \cos^{-1}(A/2\rho)$ is one-half of the sector of the circle. The triangle shown is one-half of the area that has to be subtracted to get the area to the one side of the chord. The area of the sector is $s\rho^2$. Now VR(r) can be expressed as

$$\text{VR}(r) = \frac{2\left(s\rho^2 - \dfrac{Ab}{2}\right)}{\pi\rho^2}.$$

The values of the terms in VR(r) can be expressed in terms of A, B, and r_0,

$$\rho = r_0 \tan(B/2) \quad \text{and} \quad b = \rho \sin(s).$$

Expanding terms and then simplifying gives Eq. (6),

$$\text{VR}(r) = \frac{2\left(s\rho^2 - \dfrac{Ab}{2}\right)}{\pi\rho^2} = \frac{2}{\pi}\left(s - \frac{Ab}{2\rho^2}\right)$$

$$= \frac{2}{\pi}\left\{\cos^{-1}(A/2\rho) - \frac{A\sin[\cos^{-1}(A/2\rho)]}{2r_0 \tan(B/2)}\right\}.$$

REFERENCES

Balanis, C. A., 1997: *Antenna Theory: Analysis and Design*. 2nd ed. Wiley, 941 pp.

Barrick, D. E., 1973: FM/CW radar signals and digital processing. NOAA Tech. Rep. ERL 283-WPL 26, 22 p.

Carter, D. A., K. S. Gage, W. L. Ecklund, W. M. Angevine, P. E. Johnston, A. C. Riddle, J. Wilson, and C. R. Williams, 1995: Developments in UHF lower tropospheric wind profiling at NOAA's Aeronomy Laboratory. *Radio Sci.*, **30**, 977–1001, doi:10.1029/95RS00649.

Chadwick, R. B., and R. G. Strauch, 1979: Processing of FM-CW Doppler radar signals from distributed targets. *IEEE Trans. Aerosp. Electron. Syst.*, **AES-15**, 185–189, doi:10.1109/TAES.1979.308817.

——, K. P. Moran, R. G. Strauch, G. E. Morrison, and W. C. Campbell, 1976: A new radar for measuring winds. *Bull. Amer. Meteor. Soc.*, **57**, 1120–1125, doi:10.1175/1520-0477(1976)057<1120:ANRFMW>2.0.CO;2.

Doviak, R. J., and D. S. Zrnić, 1993: *Doppler Radar and Weather Observations*. 2nd ed. Academic Press, 562 pp.

Gage, K. S., and B. B. Balsley, 1978: Doppler radar probing of the clear atmosphere. *Bull. Amer. Meteor. Soc.*, **59**, 1074–1093, doi:10.1175/1520-0477(1978)059<1074:DRPOTC>2.0.CO;2.

Harris, F. J., 1978: On the use of windows for harmonic analysis with the discrete Fourier transform. *Proc. IEEE*, **66**, 51–83, doi:10.1109/PROC.1978.10837.

Lundquist, J. D., P. J. Neiman, B. Martner, A. B. White, D. J. Gottas, and F. M. Ralph, 2008: Rain versus snow in the Sierra Nevada, California: Comparing Doppler profiling radar and surface observations of melting level. *J. Hydrometeor.*, **9**, 194–211, doi:10.1175/2007JHM853.1.

McLaughlin, S. A., 2003: A new data acquisition system for the U. S. Army FM-CW radar: Still a great way to see half-meter resolution. *12th Symp. on Meteorological Observations and Instrumentation*, Long Beach, CA, Amer. Meteor. Soc., P1.20. [Available online at https://ams.confex.com/ams/annual2003/webprogram/Paper58607.html.]

NOAA, 2015a: Hydrometeorology Testbed (HMT). Accessed 2 December 2015. [Available online at http://hmt.noaa.gov/.]

——, 2015b: Profiler network and image library. Accessed 2 December 2015. [Available online at http://www.esrl.noaa.gov/psd/data/obs/datadisplay/.]

Petitdidier, M., A. Sy, A. Garrouste, and J. Delcourt, 1997: Statistical characteristics of the noise power spectral density in UHF and VHF wind profilers. *Radio Sci.*, **32**, 1229–1247, doi:10.1029/97RS00250.

Riddle, A. C., L. M. Hartten, D. A. Carter, P. E. Johnston, and C. R. Williams, 2012: A minimum threshold for wind profiler signal-to-noise ratios. *J. Atmos. Oceanic Technol.*, **29**, 889–895, doi:10.1175/JTECH-D-11-00173.1.

Strauch, R. G., 1976: Theory and application of the FM-CW Doppler radar. Ph.D. thesis, University of Colorado, 97 pp.

Stull, R. B., 2000: *Meteorology for Scientists and Engineers*. 2nd ed. Brooks/Cole, 502 pp.

Ulbrich, C. W., and D. Atlas, 1998: Rainfall microphysics and radar properties: Analysis methods for drop size spectra. *J. Appl. Meteor.*, **37**, 912–923, doi:10.1175/1520-0450(1998)037<0912:RMARPA>2.0.CO;2.

White, A. B., J. R. Jordan, B. E. Martner, F. M. Ralph, and B. W. Bartram, 2000: Extending the dynamic range of an S-band radar for cloud and precipitation studies. *J. Atmos. Oceanic Technol.*, **17**, 1226–1234, doi:10.1175/1520-0426(2000)017<1226:ETDROA>2.0.CO;2.

——, D. J. Gottas, F. M. Ralph, and P. J. Neiman, 2001: Operational bright-band snow level detection using Doppler radar. U.S. Patent 6,615,140, filed 30 August 2001, and issued 2 September 2003.

——, ——, E. T. Strem, F. M. Ralph, and P. J. Neiman, 2002: An automated brightband height detection algorithm for use with Doppler radar spectral moments. *J. Atmos. Oceanic Technol.*, **19**, 687–697, doi:10.1175/1520-0426(2002)019<0687:AABHDA>2.0.CO;2.

——, ——, A. F. Henkel, P. J. Niman, F. M. Ralph, and S. I. Gutman, 2010: Developing a performance measure for snow-level forecasts. *J. Hydrometeor.*, **11**, 739–753, doi:10.1175/2009JHM1181.1.

——, and Coauthors, 2013: A twenty-first-century California observing network for monitoring extreme weather events. *J. Atmos. Oceanic Technol.*, **30**, 1585–1603, doi:10.1175/JTECH-D-12-00217.1.

Zhang, J., and Coauthors, 2011: National Mosaic and Multi-Sensor QPE (NMQ) system: Description, results, and future plans. *Bull. Amer. Meteor. Soc.*, **92**, 1321–1338, doi:10.1175/2011BAMS-D-11-00047.1.